FERMI LARGE AREA TELESCOPE OBSERVATIONS OF THE VELA-X PULSAR WIND NEBULA

A. A. ABDO[1,2], M. ACKERMANN[3], M. AJELLO[3], A. ALLAFORT[3], L. BALDINI[4], J. BALLET[5], G. BARBIELLINI[6,7], D. BASTIERI[8,9],
K. BECHTOL[3], R. BELLAZZINI[4], B. BERENJI[3], R. D. BLANDFORD[3], E. D. BLOOM[3], E. BONAMENTE[10,11], A. W. BORGLAND[3],
A. BOUVIER[3], J. BREGEON[4], A. BREZ[4], M. BRIGIDA[12,13], P. BRUEL[14], T. H. BURNETT[15], S. BUSON[9], G. A. CALIANDRO[16],
R. A. CAMERON[3], P. A. CARAVEO[17], S. CARRIGAN[9], J. M. CASANDJIAN[5], C. CECCHI[10,11], Ö. ÇELIK[18,19,20], A. CHEKHTMAN[1,21],
C. C. CHUNG[1,2], J. CHIANG[3], S. CIPRINI[11], R. CLAUS[3], J. COHEN-TANUGI[22], J. CONRAD[23,24,55], A. DE ANGELIS[25], F. DE PALMA[12,13],
M. DORMODY[26], E. DO COUTO E SILVA[3], P. S. DRELL[3], R. DUBOIS[3], D. DUMORA[27,28], C. FARNIER[22], C. FAVUZZI[12,13], S. J. FEGAN[14],
W. B. FOCKE[3], P. FORTIN[14], M. FRAILIS[25], Y. FUKAZAWA[29], S. FUNK[3,56], P. FUSCO[12,13], F. GARGANO[13], N. GEHRELS[18,30,31],
S. GERMANI[10,11], G. GIAVITTO[6,7], N. GIGLIETTO[12,13], F. GIORDANO[12,13], T. GLANZMAN[3], G. GODFREY[3], I. A. GRENIER[5],
M.-H. GRONDIN[27,28,56], J. E. GROVE[1], L. GUILLEMOT[27,28,57], S. GUIRIEC[32], A. K. HARDING[18], M. HAYASHIDA[3], E. HAYS[18],
D. HORAN[14], R. E. HUGHES[33], M. S. JACKSON[24,34], G. JÓHANNESSON[3], A. S. JOHNSON[3], T. J. JOHNSON[18,31], W. N. JOHNSON[1],
S. JOHNSTON[35], T. KAMAE[3], H. KATAGIRI[29], J. KATAOKA[36], N. KAWAI[37,38], M. KERR[15], J. KNÖDLSEDER[39], J. KUSS[4], J. LANDE[3],
L. LATRONICO[4], S.-H. LEE[3], M. LEMOINE-GOUMARD[27,28,56], M. LLENA GARDE[23,24], F. LONGO[6,7], F. LOPARCO[12,13], B. LOTT[27,28],
M. N. LOVELLETTE[1], P. LUBRANO[10,11], A. MAKEEV[1,21], M. MARELLI[17], M. N. MAZZIOTTA[13], J. E. MCENERY[18,31], C. MEURER[23,24],
P. F. MICHELSON[3], W. MITTHUMSIRI[3], T. MIZUNO[29], A. A. MOISEEV[19,31], C. MONTE[12,13], M. E. MONZANI[3], A. MORSELLI[40],
I. V. MOSKALENKO[3], S. MURGIA[3], T. NAKAMORI[37], P. L. NOLAN[3], J. P. NORRIS[41], A. NOUTSOS[42], E. NUSS[22], T. OHSUGI[29],
N. OMODEI[4], E. ORLANDO[43], J. F. ORMES[41], M. OZAKI[44], D. PANEQUE[3], J. H. PANETTA[3], D. PARENT[27,28], V. PELASSA[22],
M. PEPE[10,11], M. PESCE-ROLLINS[4], M. PIERBATTISTA[5], F. PIRON[22], T. A. PORTER[26], S. RAINÒ[12,13], R. RANDO[8,9], P. S. RAY[1],
N. REA[16,45], A. REIMER[3,46], O. REIMER[3,46], T. REPOSEUR[27,28], S. RITZ[26], A. Y. RODRIGUEZ[16], R. W. ROMANI[3,56], M. ROTH[15],
F. RYDE[24,34], H. F.-W. SADROZINSKI[26], D. SANCHEZ[14], A. SANDER[33], P. M. SAZ PARKINSON[26], J. D. SCARGLE[47], C. SGRÒ[4],
E. J. SISKIND[48], D. A. SMITH[27,28], P. D. SMITH[33], G. SPANDRE[4], P. SPINELLI[12,13], M. S. STRICKMAN[1], D. J. SUSON[49], H. TAJIMA[3],
H. TAKAHASHI[29], T. TAKAHASHI[44], T. TANAKA[3], J. B. THAYER[3], J. G. THAYER[3], D. J. THOMPSON[18], L. TIBALDO[5,8,9],
D. F. TORRES[16,50], G. TOSTI[10,11], A. TRAMACERE[3,51], Y. UCHIYAMA[3], T. L. USHER[3], A. VAN ETTEN[3,56], V. VASILEIOU[19,20],
C. VENTER[18,52], N. VILCHEZ[39], V. VITALE[40,53], A. P. WAITE[3], P. WANG[3], P. WELTEVREDE[42], B. L. WINER[33], K. S. WOOD[1],
T. YLINEN[24,34,54], AND M. ZIEGLER[26]

[1] Space Science Division, Naval Research Laboratory, Washington, DC 20375, USA
[2] National Research Council Research Associate, National Academy of Sciences, Washington, DC 20001, USA
[3] W. W. Hansen Experimental Physics Laboratory, Kavli Institute for Particle Astrophysics and Cosmology, Department of Physics and SLAC National Accelerator
Laboratory, Stanford University, Stanford, CA 94305, USA; ave@stanford.edu, rwr@astro.stanford.edu, funk@slac.stanford.edu
[4] Istituto Nazionale di Fisica Nucleare, Sezione di Pisa, I-56127 Pisa, Italy
[5] Laboratoire AIM, CEA-IRFU/CNRS/Université Paris Diderot, Service d'Astrophysique, CEA Saclay, 91191 Gif sur Yvette, France
[6] Istituto Nazionale di Fisica Nucleare, Sezione di Trieste, I-34127 Trieste, Italy
[7] Dipartimento di Fisica, Università di Trieste, I-34127 Trieste, Italy
[8] Istituto Nazionale di Fisica Nucleare, Sezione di Padova, I-35131 Padova, Italy
[9] Dipartimento di Fisica "G. Galilei," Università di Padova, I-35131 Padova, Italy
[10] Istituto Nazionale di Fisica Nucleare, Sezione di Perugia, I-06123 Perugia, Italy
[11] Dipartimento di Fisica, Università degli Studi di Perugia, I-06123 Perugia, Italy
[12] Dipartimento di Fisica "M. Merlin" dell'Università e del Politecnico di Bari, I-70126 Bari, Italy
[13] Istituto Nazionale di Fisica Nucleare, Sezione di Bari, 70126 Bari, Italy
[14] Laboratoire Leprince-Ringuet, École polytechnique, CNRS/IN2P3, Palaiseau, France
[15] Department of Physics, University of Washington, Seattle, WA 98195-1560, USA
[16] Institut de Ciencies de l'Espai (IEEC-CSIC), Campus UAB, 08193 Barcelona, Spain
[17] INAF-Istituto di Astrofisica Spaziale e Fisica Cosmica, I-20133 Milano, Italy
[18] NASA Goddard Space Flight Center, Greenbelt, MD 20771, USA
[19] Center for Research and Exploration in Space Science and Technology (CRESST) and NASA Goddard Space Flight Center, Greenbelt, MD 20771, USA
[20] Department of Physics and Center for Space Sciences and Technology, University of Maryland Baltimore County, Baltimore, MD 21250, USA
[21] George Mason University, Fairfax, VA 22030, USA
[22] Laboratoire de Physique Théorique et Astroparticules, Université Montpellier 2, CNRS/IN2P3, Montpellier, France
[23] Department of Physics, Stockholm University, AlbaNova, SE-106 91 Stockholm, Sweden
[24] The Oskar Klein Centre for Cosmoparticle Physics, AlbaNova, SE-106 91 Stockholm, Sweden
[25] Dipartimento di Fisica, Università di Udine and Istituto Nazionale di Fisica Nucleare, Sezione di Trieste, Gruppo Collegato di Udine, I-33100 Udine, Italy
[26] Santa Cruz Institute for Particle Physics, Department of Physics and Department of Astronomy and Astrophysics, University of California at Santa Cruz,
Santa Cruz, CA 95064, USA
[27] Université de Bordeaux, Centre d'Études Nucléaires Bordeaux Gradignan, UMR 5797, Gradignan, 33175, France;
lemoine@cenbg.in2p3.fr, grondin@cenbg.in2p3.fr
[28] CNRS/IN2P3, Centre d'Études Nucléaires Bordeaux Gradignan, UMR 5797, Gradignan, 33175, France
[29] Department of Physical Sciences, Hiroshima University, Higashi-Hiroshima, Hiroshima 739-8526, Japan
[30] Department of Astronomy and Astrophysics, Pennsylvania State University, University Park, PA 16802, USA
[31] Department of Physics and Department of Astronomy, University of Maryland, College Park, MD 20742, USA
[32] Center for Space Plasma and Aeronomic Research (CSPAR), University of Alabama in Huntsville, Huntsville, AL 35899, USA
[33] Department of Physics, Center for Cosmology and Astro-Particle Physics, The Ohio State University, Columbus, OH 43210, USA
[34] Department of Physics, Royal Institute of Technology (KTH), AlbaNova, SE-106 91 Stockholm, Sweden
[35] Australia Telescope National Facility, CSIRO, Epping NSW 1710, Australia
[36] Waseda University, 1-104 Totsukamachi, Shinjuku-ku, Tokyo, 169-8050, Japan
[37] Department of Physics, Tokyo Institute of Technology, Meguro City, Tokyo 152-8551, Japan

[38] Cosmic Radiation Laboratory, Institute of Physical and Chemical Research (RIKEN), Wako, Saitama 351-0198, Japan
[39] Centre d'Étude Spatiale des Rayonnements, CNRS/UPS, BP 44346, F-30128 Toulouse Cedex 4, France
[40] Istituto Nazionale di Fisica Nucleare, Sezione di Roma "Tor Vergata," I-00133 Roma, Italy
[41] Department of Physics and Astronomy, University of Denver, Denver, CO 80208, USA
[42] Jodrell Bank Centre for Astrophysics, School of Physics and Astronomy, The University of Manchester, M13 9PL, UK
[43] Max-Planck Institut für extraterrestrische Physik, 85748 Garching, Germany
[44] Institute of Space and Astronautical Science, JAXA, 3-1-1 Yoshinodai, Sagamihara, Kanagawa 229-8510, Japan
[45] Sterrenkundig Institut "Anton Pannekoek," 1098 SJ Amsterdam, The Netherlands
[46] Institut für Astro- und Teilchenphysik and Institut für Theoretische Physik, Leopold-Franzens-Universität Innsbruck, A-6020 Innsbruck, Austria
[47] Space Sciences Division, NASA Ames Research Center, Moffett Field, CA 94035-1000, USA
[48] NYCB Real-Time Computing Inc., Lattingtown, NY 11560-1025, USA
[49] Department of Chemistry and Physics, Purdue University Calumet, Hammond, IN 46323-2094, USA
[50] Institució Catalana de Recerca i Estudis Avançats (ICREA), Barcelona, Spain
[51] Consorzio Interuniversitario per la Fisica Spaziale (CIFS), I-10133 Torino, Italy
[52] North-West University, Potchefstroom Campus, Potchefstroom 2520, South Africa
[53] Dipartimento di Fisica, Università di Roma "Tor Vergata," I-00133 Roma, Italy
[54] School of Pure and Applied Natural Sciences, University of Kalmar, SE-391 82 Kalmar, Sweden

ABSTRACT

We report on gamma-ray observations in the off-pulse window of the Vela pulsar PSR B0833−45 using 11 months of survey data from the *Fermi* Large Area Telescope (LAT). This pulsar is located in the 8° diameter Vela supernova remnant, which contains several regions of non-thermal emission detected in the radio, X-ray, and gamma-ray bands. The gamma-ray emission detected by the LAT lies within one of these regions, the $2° \times 3°$ area south of the pulsar known as Vela-X. The LAT flux is significantly spatially extended with a best-fit radius of $0°.88 \pm 0°.12$ for an assumed radially symmetric uniform disk. The 200 MeV to 20 GeV LAT spectrum of this source is well described by a power law with a spectral index of $2.41 \pm 0.09 \pm 0.15$ and integral flux above 100 MeV of $(4.73 \pm 0.63 \pm 1.32) \times 10^{-7}$ cm^{-2} s^{-1}. The first errors represent the statistical error on the fit parameters, while the second ones are the systematic uncertainties. Detailed morphological and spectral analyses give strong constraints on the energetics and magnetic field of the pulsar wind nebula system and favor a scenario with two distinct electron populations.

Key words: gamma rays: general – pulsars: general – pulsars: individual (Vela, PSR J0835–4510)

Online-only material: color figures

1. INTRODUCTION

The Vela pulsar (PSR B0833–45) at a distance of 290 pc (Dodson et al. 2003) is one of the closest pulsars to Earth and is therefore studied in great detail. Its period of 89 ms and characteristic age of $\tau_c = 11,000$ years make it an archetype of the class of adolescent pulsars. As with most other pulsars, the Vela pulsar was first detected through radio observations (Large et al. 1968) and gamma rays (Thompson et al. 1975), but later studied in detail in the optical (Wallace et al. 1977), X-ray (Harnden & Gorenstein 1973), and gamma-ray bands (Kanbach et al. 1980, 1994). The pulsar has a spin-down energy loss rate of 7×10^{36} erg s^{-1} with the peak electromagnetic power emitted in the GeV gamma-ray band. Indeed, the Vela pulsar is the brightest steady astrophysical source for the *Fermi* Large Area Telescope (LAT; Abdo et al. 2009a). The gamma-ray properties of the pulsar have been studied in detail with the *Fermi*-LAT, locating the gamma-ray emission far out in the magnetosphere close to the last open field lines.

Yet ∼99% of the pulsar spin-down luminosity is not observed as pulsed photon emission and is apparently carried away as a magnetized particle wind. Radio and X-ray observations established the presence of large-scale diffuse emission surrounding PSR B0833–45, thought to be related to the Vela supernova remnant (SNR; Dwarakanath 1991; Duncan et al. 1996; Aschenbach et al. 1995). These radio observations show that the

roughly 8° diameter Vela SNR (Aschenbach et al. 1995) contains three distinct central regions of bright diffuse emission, dubbed Vela-X, Vela-Y, and Vela-Z (Rishbeth 1958). The most intense of these, Vela-X, is an extremely bright (∼1000 Jy) diffuse radio structure of size 2°–3° located close to PSR B0833−45. Its radio spectral index is significantly harder than those of Vela-Y and Vela-Z, pointing to a young population of non-thermal electrons. Indeed, the flat radio spectral index, the proximity to the Vela pulsar, and the large degree of radio polarization in Vela-X led Weiler & Panagia (1980) to first suggest that the diffuse radio emission is a pulsar wind nebula (PWN) formed by a relativistic outflow powered by the spin-down of PSR B0833−45. The deceleration of the pulsar-driven wind as it sweeps up ejecta from the supernova explosion generates a termination shock at which the particles are pitch-angle scattered and further accelerated to ultrarelativistic energies. The PWN emission extends across the electromagnetic spectrum in synchrotron and inverse Compton (IC) components from radio to TeV energies (Gaensler & Slane 2006). PWNe studies can supply information on particle acceleration in shocks, on evolution of the pulsar spin-down, and on the ambient interstellar gas.

High angular resolution observations of Vela-X in different wave bands showed a rather complex morphology. X-ray images taken with the *Chandra X-ray Telescope* revealed further details (Helfand et al. 2001): two toroidal arcs of emission, 17″ and 30″ away from the pulsar, and a 4′ long collimated feature along the pulsar spin axis, which is interpreted as a jet. These structures are embedded in an extended nebula located to the south of the Vela pulsar and observed in soft X-rays with the *ROSAT* X-ray telescope. This bright X-ray and radio structure, usually referred to as the "cocoon," has an extension of ∼0°.5 × 1°.5
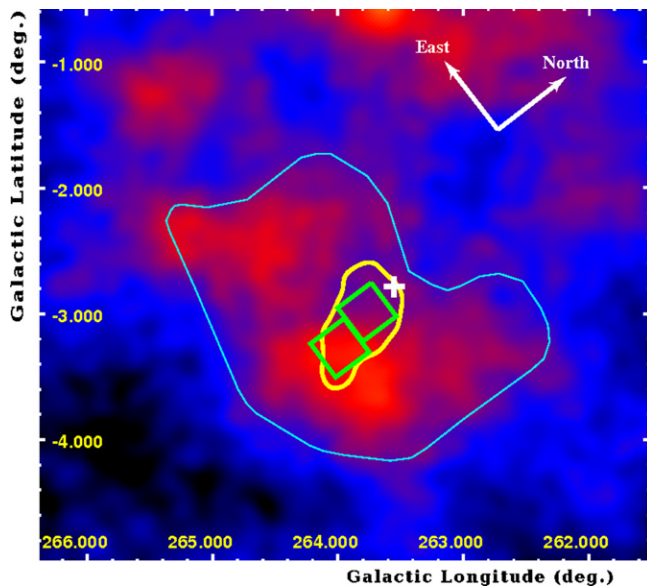
Figure 1. 61 GHz *Wilkinson Microwave Anisotropy Probe* (*WMAP*; archival data) radio sky map of Vela-X in galactic coordinates. The position of the Vela pulsar is marked with a cross. The blue outer contour shows the region where the integral flux densities and the spectral indices were computed for the radio data. The extraction regions for the spectral analysis of the *ASCA* data are delimited with green boxes. The yellow inner line presents the H.E.S.S. contour at 68% of the peak value.

(A color version of this figure is available in the online journal.)

and is generally thought to represent PWN flow crushed by the passage of the SNR reverse shock. The offset of the cocoon to the south of the pulsar is explained by dense material to the north of PSR B0833−45 that prevents a symmetric expansion of the PWN (Blondin et al. 2001). The X-ray spectrum of the cocoon shows a thermal component with a high-energy power-law tail. The detection of very high energy (VHE) gamma-ray emission (Aharonian et al. 2006) in the cocoon region, albeit at larger angular scales ($58' \times 43'$; yellow inner contour in Figure 1), clearly confirmed the notion of a non-thermal particle population in this structure. However, these particles do not easily explain the larger and brighter Vela-X radio emission in the surrounding "halo" (blue outer contour in Figure 1). This led de Jager et al. (2008) to suggest a model with two populations of electrons: one at high energies located on the smaller cocoon scale, responsible for the X-ray and TeV emission, and a second lower energy population extending to larger scales and producing the radio flux. These models made a clear prediction that the radio-emitting electrons should be visible in the LAT band through IC scattering of the radio-emitting electrons off ambient photon fields. EGRET, the predecessor of the *Fermi*-LAT, was only able to place upper limits on non-pulsed emission from this region (Kanbach et al. 1994). Recently, using the *AGILE* satellite, Pellizzoni et al. (2010) reported the detection of the Vela PWN in the energy range from 100 MeV to 3 GeV.

Here, we report on detection of a significant signal in the Vela pulsar off-pulse emission using 11 months of survey observations with the *Fermi*-LAT.

2. LAT DESCRIPTION AND OBSERVATIONS

The LAT is a gamma-ray telescope that detects photons by conversion into electron–positron pairs and operates in the energy range between 20 MeV and 300 GeV. It is made of a high-resolution converter tracker (direction measurement of the incident gamma rays), a CsI(Tl) crystal calorimeter (energy measurement), and an anti-coincidence detector to identify the background of charged particles (Atwood et al. 2009). In comparison to EGRET, the LAT has a larger effective area ($\sim$8000 cm² on-axis above 1 GeV), a broader field of view (FOV; $\sim$2.4 sr), and a superior angular resolution ($\sim0°.6$ 68% containment at 1 GeV for events converting in the front section of the tracker). Details of the instruments and data processing are given in Atwood et al. (2009). The on-orbit calibration is described in Abdo et al. (2009a).

The following analysis was performed using 11 months of data collected starting 2008 August 4 and extending until 2009 July 4. Only gamma rays in the *Diffuse* class events were selected (with the tightest background rejection), and from this sample, we excluded those coming from a zenith angle larger than 105° to the detector axis because of the possible contamination from Earth albedo photons. We have used P6_V3 post-launch instrument response functions (IRFs) that take into account pile-up and accidental coincidence effects in the detector subsystems.[58]

3. TIMING SOLUTION

The Vela pulsar is the brightest persistent point source in the gamma-ray sky with pulsed photons observed up to 25 GeV. The study of Vela-X thus requires us to assign a phase to the gamma-ray photons and select those in an off-pulse window. Since the Vela pulsar is young and exhibits substantial timing irregularities, phase assignment generally requires a contemporary radio ephemeris; such a timing model is produced from observations made with the Parkes 64 m radio telescope. However, Vela is sufficiently bright to be timed directly in the gamma rays; for this work and that reported in Abdo et al. (2010), we chose to use a timing model derived directly from LAT observations. We used six gamma-ray times of arrival (TOA) covering the commissioning phase of the mission (2008 June 25 through August 4) at 5 day intervals and 24 TOAs spaced at 2 week intervals during the survey portion of the mission (2008 August 4 through 2009 July 15). The TOAs were fitted to a timing model using TEMPO2; the rms residuals of the TOAs with respect to the fitted model are 63 μs. More details can be found in Abdo et al. (2010). Pulse phases were assigned to the LAT data using the *Fermi* plug-in provided by the LAT team and distributed with TEMPO2. As shown in Figure 1 of Abdo et al. (2009a) the pulsar emission is quite faint in the phase interval $\phi = 0.7$–1.0. We have used this phase interval for both the spectral and morphological analysis.

4. RESULTS

The spatial and spectral analysis of the gamma-ray emission was performed using two different methods. The first is a maximum likelihood method (Mattox et al. 1996) implemented in the *Fermi* SSC science tools as the "gtlike" code. The second is an analysis tool developed by the LAT team called "Sourcelike." In the latter, likelihood fitting is iterated to the data set to simultaneously optimize the position and the extension of a source, assuming spatially extended source models and taking into account nearby sources as well as Galactic diffuse and isotropic components in the fits. Here, we tried both point source and uniform disk models. Sourcelike can also be used to assess the test statistic (TS) value and to compute the spectra of both

---

[58] See http://fermi.gsfc.nasa.gov/ssc/data/analysis/documentation/Cicerone/Cicerone_LAT_IRFs/IRF_overview.html for more details.
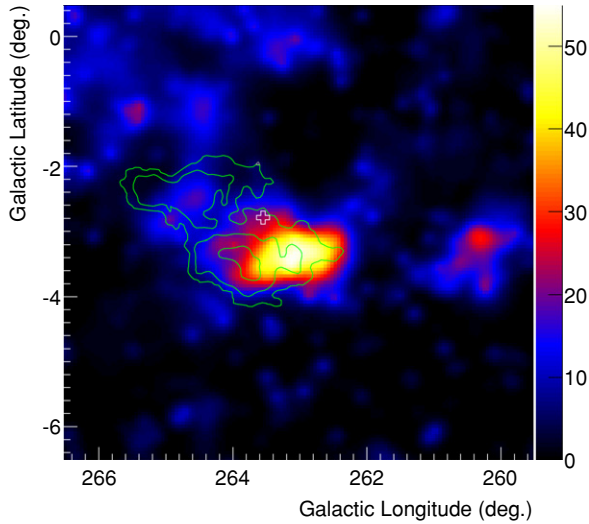
Figure 2. Test statistic (TS) map of the PWN Vela-X with side length 7° above 800 MeV. Each pixel of this image contains the TS value for the assumption of a point source located at the pixel position. *WMAP* radio contours at 61 GHz (archival data, see Section 4.3) are overlaid as green solid lines. The position of the Vela pulsar, PSR B0833−45, is indicated with a white cross. An unidentified source, coincident with the northeastern part of Puppis A is visible at position $(l, b) = (260.30, −3.16)$.

(A color version of this figure is available in the online journal.)

extended and point-like sources. In this method, the maximum likelihood is performed in independent energy bands, using a region of interest whose size is energy dependent: from 15° at 200 MeV to 3.5 at 50 GeV.

We used the map cube file gll_iem_v02.fit to model the Galactic diffuse emission together with the corresponding tabulated model isotropic_iem_v02.txt for the extragalactic diffuse and the residual instrument emissions.[59] Other versions of the Galactic diffuse models, generated by GALPROP, are also used to assess systematic errors as discussed in Section 4.2. Nearby sources in the FOV with a statistical significance larger than 5σ are extracted as described in Abdo et al. (2009b) and taken into account in the study.

4.1. Morphology

In the study of the morphology of an extended source, a major requirement is to have the best possible angular resolution. Therefore, we decided to restrict our LAT data set to events with energies above 800 MeV, which further reduces the Galactic diffuse background. Figure 2 presents the LAT TS map of off-pulse emission in the Vela region. The TS is defined as twice the difference between the log-likelihood L_1 obtained by fitting a source model plus the background model to the data, and the log-likelihood L_0 obtained by fitting the background model only, i.e., TS $= 2(L_1 - L_0)$. This sky map contains the TS value for a point source at each map location, thus giving a measure of the statistical significance for the detection of a gamma-ray source in excess of the background. Note that the pulsar (cross) is quite faint in this phase interval. The sky map shows bright emission south of PSR B0833−45 with a fainter extension to the east. This gamma-ray complex lies within Vela-X; in particular it is contained within the region that remains strong at high radio frequencies (denoted by the *WMAP* flux contours, see discussion). An additional source, still unidentified
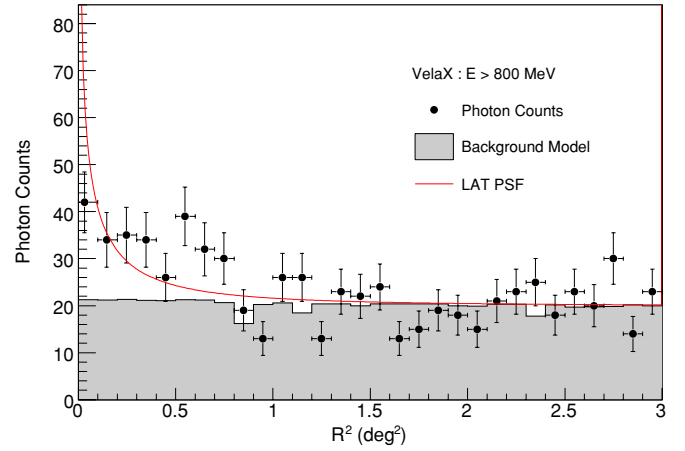
Figure 3. Radial profile of the LAT data about the best-fit position provided by Sourcelike for a point source $(l, b) = (263.03, −3.27)$ as reported in Table 1 $(E > 800$ MeV). The LAT PSF is overlaid as a red solid line for comparison. The background model is presented as a gray histogram and the black dots represent the LAT data.

(A color version of this figure is available in the online journal.)

Table 1
Centroid and Extension Fits to the LAT Data for Vela-X using Sourcelike for Events with Energies above 800 MeV

Model	Name	Energy Band (GeV)	l (deg)	b (deg)	Radius (deg)	ΔTS
Point source	PS	0.8–20.0	263.03	−3.27		
Disk	D	0.8–20.0	263.34	−3.11	0.88 ± 0.12	47.9

but coincident with the northeastern part of the SNR Puppis A, is also visible at position $(l, b) = (260.30, −3.16)$ with a TS value of 34.6. This source is taken into account in the spectral analysis.

We determined the source extension using Sourcelike with a uniform disk hypothesis (compared to the point-source hypothesis). The results of the extension fits are summarized in Table 1. The difference in TS between the uniform disk and the point-source hypothesis is 47.9 (which converts into a significance of ∼7σ for the source extension) for 800 MeV < E < 20 GeV, which demonstrates that the source is significantly extended with respect to the LAT point-spread function (PSF). The fit extension has a radius of 0.88 ± 0.12. We support this conclusion in Figure 3, showing the radial profile for the LAT data above 800 MeV (from the best source location determined for a point-source fit) and comparing this with the LAT PSF.

We have also examined the correspondence of the gamma-ray emission with different source morphologies by using gtlike with assumed multi-frequency templates. For this exercise, we compared the TS of the point source and uniform model parameters provided by Sourcelike with values derived when using morphological templates from the H.E.S.S. gamma-ray excess map (Aharonian et al. 2006) and the *WMAP* radio images at 61 GHz (archival data, see Section 4.3). The resulting TS values obtained from our maximum likelihood fitting are summarized in Table 2. Fitting a uniform disk to the data using the best location and size provided by Sourcelike improves the TS by 40.4 in comparison to the point-source hypothesis, comparable to the improvement in TS between D and PS models in Table 1. Replacing the disk with spatial template provided by the H.E.S.S. observations decreases the TS with respect to the disk hypothesis (ΔTS $= −31.3$), implying that the LAT emission does not correspond well to the TeV flux. In contrast, using the

Table 2
Comparison of Model Likelihood Fitting Results with Gtlike for Events with
Energies above 800 MeV

Model	Name	TS
Point source	PS	44.0
Disk	D	84.4
H.E.S.S.		53.1
WMAP 61 GHz		94.0

Note. For each model, we give the name and the TS value.

radio contours as spatial template improves the value of the TS, but only by ΔTS = +11.7. Thus, while the best match is with the radio morphology, as expected from the double electron population scenario, we cannot (at high significance) rule out a simple disk morphology.

4.2. Spectral Analysis

The *Fermi*-LAT spectral points were obtained by dividing the 200 MeV to 20 GeV range into seven logarithmically spaced energy bins and performing a maximum likelihood spectral analysis in each interval, assuming a power-law shape for the source. For this analysis, we used the uniform disk model from Table 1 to represent the gamma-ray emission observed by the LAT, as discussed in Section 4.1. Assuming this spatial shape, the gamma-ray source observed by the LAT is detected with a significance of 14σ in the 200 MeV to 20 GeV range. The result, renormalized to the total phase interval, is presented in Figure 4. To determine the integrated gamma-ray flux, we fit a power-law spectral model to the data in the energy range 200 MeV to 20 GeV with a maximum likelihood analysis. This analysis is more reliable than a direct fit to the spectral points of Figure 4 since it accounts for Poisson statistics of the data. The spectrum of Vela-X between 200 MeV and 20 GeV, assuming the uniform disk model from Table 1, is well described by a power law with a spectral index of $2.41 \pm 0.09 \pm 0.15$ and an integral flux above 100 MeV of $(4.73 \pm 0.63 \pm 1.32) \times 10^{-7} \, \mathrm{cm}^{-2} \, \mathrm{s}^{-1}$ (renormalized to the full phase interval). This is in agreement with results obtained independently using Sourcelike. The first error is statistical, while the second represents our estimate of systematic effects as discussed below. No indication of a spectral cutoff at high energy can be detected with the current statistics. This result takes into account the gamma-ray emission from the source coincident with Puppis A, which was well modeled as a point source emitting a power law of spectral index 1.97 ± 0.16 and integral flux above 100 MeV of $(0.43 \pm 0.16) \times 10^{-7} \, \mathrm{cm}^{-2} \, \mathrm{s}^{-1}$ (statistical errors only).

As an attempt to estimate the level of pulsed emission in the off-pulse window, we fitted a point source at the position of the Vela pulsar, in addition to the uniform disk representing Vela-X. We derived an integral flux above 100 MeV of $\sim 3 \times 10^{-8} \, \mathrm{cm}^{-2} \, \mathrm{s}^{-1}$ for the point source, which represents $\sim 6\%$ of the flux of Vela-X.

Fitting a point source only at the position of the Vela pulsar, we get a spectrum well described by a power law with a spectral index of 2.98 ± 0.16 and an integral flux above 100 MeV of $(1.48 \pm 0.25) \times 10^{-7} \, \mathrm{cm}^{-2} \, \mathrm{s}^{-1}$ for the phase interval 0.7–1.0 (statistical errors only). This low flux is in agreement with the upper limit reported in Abdo et al. (2009a).

Three different systematic uncertainties can affect the LAT flux estimation. The main systematic at low energy is due to the uncertainty in the Galactic diffuse emission since Vela-X is located only $2°$ from the Galactic plane in a region of dense
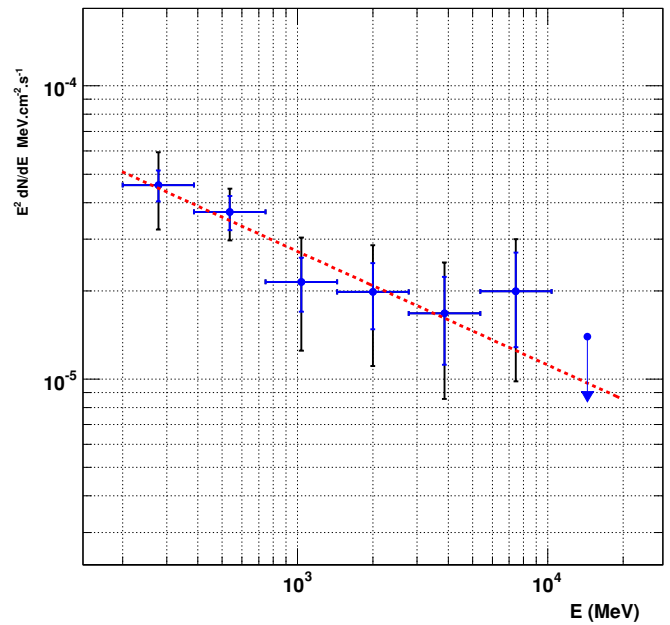

Figure 4. Spectral energy distribution of Vela-X renormalized to the total phase interval. The LAT spectral points are obtained using the maximum likelihood method described in Section 4.2 into seven logarithmically spaced energy bins. The statistical errors are shown in blue, while the black lines take into account both the statistical and systematic errors as discussed in Section 4.2. The red dotted line presents the result obtained by fitting a power law to the data in the 200 MeV to 20 GeV energy range using a maximum likelihood fit. A 95% C.L. upper limit is computed when the statistical significance is lower than 3σ.

(A color version of this figure is available in the online journal.)

molecular clouds. Different versions of the Galactic diffuse emission generated by GALPROP were used to estimate this error. The difference with the best-fit diffuse model is found to be $\leqslant 6\%$. By changing the normalization of the Galactic diffuse model artificially by $\pm 6\%$, we estimate this systematic error to be 25% (0.2–0.4 GeV), 14% (0.4–0.8 GeV), and $<10\%$ (>0.8 GeV). The second systematic is related to the morphology of the LAT source. The fact that we do not know the true gamma-ray morphology introduces another source of error that becomes dominant when the size of the source is larger than the PSF, i.e., above 600 MeV for the case of Vela-X. Different spatial shapes have been used to estimate this systematic error: a disk, a Gaussian, and the radio templates. Our estimate of this uncertainty is $\sim 25\%$ between 600 MeV and 1 GeV and 30% above 1 GeV. The third uncertainty, common to every source analyzed with the LAT data, is due to the uncertainties in the effective area. This systematic is estimated by using modified IRFs whose effective area bracket that of our nominal IRF. These "biased" IRFs are defined by envelopes above and below the nominal dependence of the effective area with energy by linearly connecting differences of (10%, 5%, and 20%) at log(E) of (2, 2.75, and 4) respectively. We combine these various errors in quadrature to obtain our best estimate of the total systematic error at each energy and propagate through to the fit model parameters.

4.3. Supporting Multi-wavelength Measurements

As a means of better understanding the Vela PWN, we compiled and analyzed multi-wavelength data corresponding to the longer wavelength synchrotron counterparts of the sub-GeV-peak (halo) and TeV-peak (cocoon) Compton emission. Although their morphologies do vary with wave band, we have

attempted to form the spectral energy distributions (SEDs) of the halo and cocoon of Vela-X by using consistent apertures. This is important in this complex region and has, apparently, not been the practice in some previous studies. Vela-X itself has been traditionally studied at low radio frequencies where the spatial resolution is very poor. However, in an 8.4 GHz Parkes image (Figure 2 of Hales et al. 2004), a ~2°.5 × 1°.5 region of bright filamentary emission is visible, roughly coincident with the extended LAT flux. We examined archival 5 year (*WMAP*) sky maps[60] and find that this region appears as a distinct concentration in the *WMAP* all-sky images at 23, 33, 41, 61, and 94 GHz. As the resolution increases to higher frequencies it is increasingly separated into eastern and western sub-regions, both well south of the Vela pulsar. We measured a flux for each energy band and estimated a flux error (dominated by the uncertainty in the background estimation) using the region defined in Figure 1. This concentration is also clear in the 0.4 GHz all-sky maps of Haslam et al. (1982), which provide a low-frequency point. The flux measurements are plotted in Figure 5. We were not able to extract a reliable flux estimate from the 8.4 GHz map. We estimate the flux density spectral index for this region of Vela-X as $\alpha = 0.5 \pm 0.05$, similar to but steeper than the $\alpha = 0.39 \pm 0.03$ index measured over 0.03–8 GHz for a much larger region covering all of Vela-X (Alvarez et al. 2001). The component measured here is ~5× fainter. Additional millimeter and IR measurements would be very helpful in extending the spectrum and searching for the expected synchrotron peak at ~millimeter wavelengths.

In the X-ray band many authors have estimated the spectrum of the cocoon region, starting with the *ROSAT* analysis of Markwardt & Ogelman (1995). More detailed fitting with *ASCA* (Markwardt & Ogelman 1997; Horns et al. 2006) showed that the emission must consist of an optically thin thermal plasma (typically a mekal thermal plasma model) with $kT \approx 0.3$ keV plus a power law ($\Gamma \approx 2.0 \pm 0.3$) component. More recently, LaMassa et al. (2008) have analyzed *XMM-Newton* data of the bright central portion of the cocoon and fit a thermal plasma ($kT = 0.48^{+0.05}_{-0.06}$ keV) plus power law ($\Gamma = 2.3 \pm 0.04$). The 0.2–6.5 keV power-law flux that they find corresponds to $(9.5 \pm 1.2) \times 10^{-11}$ erg cm^{-2} s^{-1}, when scaled up to the area of the bright H.E.S.S. emission considered here. These authors also fit a hydrogen column density of $n_H = 1.6^{+0.3}_{-0.2} \times 10^{20}$ cm^{-2}, which we shall adopt for our analysis. All of the analyses extending above 2 keV have been forced to measure only portions of the long ~1°.5 cocoon structure. A number of older X-ray (Einstein, Harnden et al. 1985; HEAOA-4, Levine et al. 1984) and soft gamma ray (OSSE, de Jager et al. 1996; *BeppoSAX*, Mangano et al. 2005) observations of the Vela plerion possess a large enough FOV to encompass the majority of Vela-X. Yet the spectral extraction regions of these observations are centered on the Vela pulsar, such that the bright inner PWN contaminates the low surface brightness extended nebula and hardens the net spectrum. We therefore refrain from using such archival data as an estimate of the Vela-X spectrum.

We made a first attempt to improve such measurements by fitting to the combined emission in several *ASCA* GIS2/3 pointings that cover the bulk of the cocoon, as presented in Figure 1. Data set 25038000 (76 ks livetime) covered the northern region while data sets 23043000 and 23043010 (combined livetime 134 ks) cover the southern region. Using XSelect version 2.4, we extract data sets from two 20′ × 20′
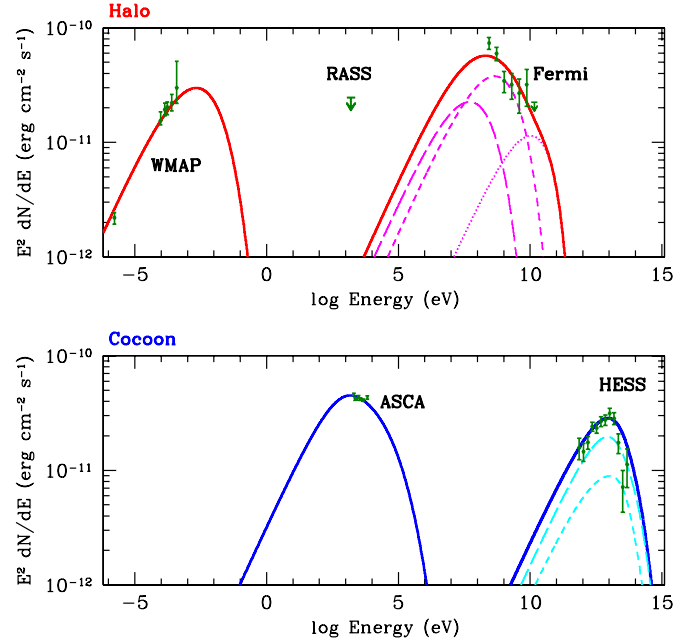
Figure 5. Spectral energy distribution of regions within Vela-X from radio to very high energy gamma rays. Upper panel: emission from the low-energy electron population (halo). *WMAP* and GeV gamma-ray points (this paper) are for the large radio-bright portion of Vela-X. The *ROSAT* upper limit (this paper) on the soft X-ray flux of this region is also shown by an arrow. The Compton components from scattering on the CMB (magenta long dashed line), dust emission (magenta dashed line) and starlight (magenta dotted line) are shown. Lower panel: synchrotron and Compton emission from the high-energy electron population (cocoon). X-ray (*ASCA* observations, this paper) and very high energy gamma-ray (Aharonian et al. 2006) points are also from the cocoon region. Only CMB (cyan long dashed line) and dust (cyan dashed line) scattered flux is shown as the starlight is Klein–Nishina suppressed.

(A color version of this figure is available in the online journal.)

regions, one each in the north and south which largely covered this region. The large GIS FOV allowed us to select background regions well outside of the cocoon but on the same detector. We assumed a fixed absorption $n_H = 1.6 \times 10^{20}$ cm^{-2} and fit a mekal thermal plasma plus power law to the combined data. The thermal component is fit with $kT = 0.51^{+0.05}_{-0.04}$ keV (single parameter 90% errors) over all data sets; no significant variation is seen in kT for independent fits to the northern and southern regions. To best constrain the power-law component, we restricted the fit to the 2–10 keV range—here separate fits gave $\Gamma = 1.97^{+0.06}_{-0.05}$ in the north and a slightly softer 2.15 ± 0.10 in the south, providing weak evidence for aging of the electron population as one moves along the cocoon. Finally for comparison with the H.E.S.S. emission, we fit to the combined regions, obtaining an average index of 2.06 ± 0.05 and 2–10 keV flux of $(6.7 \pm 0.4) \times 10^{-11}$ erg cm^{-2} s^{-1} (scaling up the flux in our extraction aperture to the area of the bright H.E.S.S. emission). This corresponds to a 0.3–7 keV flux of $(1.4 \pm 0.1) \times 10^{-10}$ erg cm^{-2} s^{-1} in good agreement with previous estimates. The SED points from the 2–10 keV power-law portion of this fit are plotted in Figure 5.

Finally, we wish to check for X-ray emission from the larger halo portion of Vela-X covered by the radio/LAT component. This very large region is presently well covered only by the *ROSAT* All-Sky Survey (RASS), which is strongly dominated by the bright thermal emission of the Vela SNR, particularly at low energy. To produce a bound on the flux, we measured the counts within the radio/LAT region in the

hard-band 0.5–2.0 keV RASS image, subtracting background from appropriate surrounding regions. No significant excess counts were found and we convert the upper bound on the flux of a $\Gamma = 2$ power-law component using WebPIMMS, obtaining 2.5×10^{-11} erg cm^{-2} s^{-1}. This bound is shown by an arrow in Figure 5.

5. DISCUSSION

Different scenarios have been proposed to interpret the multi-wavelength observations of Vela-X. Horns et al. (2006) proposed a hadronic model wherein the gamma-ray emission is the result of the decay of neutral pions produced in proton–proton collisions in the cocoon. However, this model requires a particle density larger than 0.6 cm^{-3}, which seems disfavored by the recent best-fit estimate of thermal particle density of ∼0.1 cm^{-3} using *XMM-Newton* observations (LaMassa et al. 2008). LaMassa et al. (2008) proposed a leptonic model with radio and X-ray emissions resulting from synchrotron radiation and gamma-ray emission arising from IC scattering. In this model, the authors need a three-component broken power law to describe the electron population and adequately fit the data. A model with a single break can also reproduce the multi-wavelength data if a separate electron population produces the radio emission (de Jager et al. 2008). In this case, the morphology of the gamma-ray emission observed by *Fermi* should be similar to that in the radio since they are produced by the same electron population. In the model of de Jager et al. (2008), the low-energy electron component has a total energy of 4×10^{48} erg, while the X-ray/TeV-peak component has a total lepton energy of 2×10^{46} erg. Both employ a magnetic field of 5 μG.

Our new *Fermi*-LAT spectrum and the improved flux estimates for the radio and X-ray emission from the two components of our SED (Figure 5) allow considerable progress in constraining the model parameters. First, the steep LAT spectrum disfavors the hadronic scenario. While the VHE gamma-ray data can be adequately fit with gammas from pion decay, neither the *ASCA* nor the LAT data can be accounted for by secondary electrons. We therefore require a three-component injection (one hadron and two lepton) in this case, along with a quite high magnetic field in the cocoon in order to suppress IC scattering of X-ray emitting electrons from providing the dominant source of VHE gamma rays. As noted by de Jager et al. (2008), the SED strongly supports a two-component leptonic model. We have computed the SEDs from evolving power-law electron populations, one each for the X-ray/VHE-peak cocoon and radio/sub-GeV-peak halo. In both regions an exponentially cutoff power law is injected at constant luminosity and evolved for the 11 kyr estimated lifetime of the Vela pulsar, subject to synchrotron and Klein–Nishina adjusted Compton losses. We ignore any possible adiabatic losses to the electron population, since these are quite uncertain and may, in any case, be offset by the compression from the SNR reverse shock. IC seed fields include cosmic microwave background (CMB), far IR (temperature 25 K, density 0.4 eV cm^{-3}) and starlight (temperature 6500 K, density 0.4 eV cm^{-3}; de Jager et al. 2008), reasonable for the locale of Vela-X (Porter et al. 2006). For each region, we vary the magnetic field, power-law cutoff energy, power-law index, and total lepton energy; we find the best-model fit by minimizing the weighted chi-squared statistic between model and data points. For each parameter 90% one-dimensional errors are subsequently calculated by varying the best-fit value of the given parameter until chi-squared increases by 2.71. The $\alpha = 0.5$ halo

Table 3
Multi-wavelength SED Fit to the PWN Components as Seen in Figure 5

Component	B (μG)	E_c (eV)	Γ	E_{tot} (erg)	χ^2/dof
Halo	$3.93^{+0.46}_{-0.38}$	$1.01^{+0.07}_{-0.13} \times 10^{11}$	$1.97^{+0.02}_{-0.02}$	$5.05^{+0.45}_{-0.56} \times 10^{48}$	10.7/9
Cocoon	$3.80^{+0.10}_{-0.08}$	$5.69^{+0.16}_{-0.33} \times 10^{14}$	$1.998^{+0.003}_{-0.001}$	$1.50^{+0.01}_{-0.05} \times 10^{46}$	57.7/15

radio spectral index suggests an electron power-law index close to the classical $p = 2\alpha + 1 = 2$. The synchrotron/Compton peak ratio of the cocoon implies a $B = 4 \, \mu$G field, with small uncertainty. In fact, we adequately match the SED of both components with this field and an E^{-2} spectrum. However, for the cocoon region we require a 600 TeV exponential cutoff and total energy 1.5×10^{46} erg, while the halo requires a lower 100 GeV exponential cutoff and a total energy of 5×10^{48} erg. The peaks of the cocoon component are controlled by the cooling break. The halo population does not cool appreciably during the pulsar lifetime and the peak energies are controlled by the exponential cutoff of the injected spectrum. The X-ray upper limit on this component is not constraining. Note that we do not require a mid-range break in the injected spectrum for either component.

With so many free parameters, such SED fits are usually illustrative, rather than constraining. However, with our new LAT detection and improved low energy measurements we are testing the plausible injection spectrum for the Vela-X PWN. We list the parameters determined by chi-squared fits to the multi-wavelength data and single-parameter fit errors in Table 3. The cocoon emission evidently represents significantly cooled electrons, dominated by relatively recent injection of high-energy electrons from the pulsar and its termination shock. The halo component, on the other hand, represents old electrons—these are easily produced over the lifetime of the pulsar for any initial spin period ⩽60 ms. Although it would be very interesting to push the LAT spectral measurement to lower energy, where the halo spectrum may peak, this will prove very difficult even with more exposure, given the poor low energy PSF. On the other hand, extension of the radio spectrum through the millimeter band promises to constrain the high energy cutoff of the halo electron spectrum. For the cocoon component, scheduled *XMM-Newton* mapping of this region should provide appreciable improvement in the spectral measurements of the nonthermal X-rays and may extend to low enough energy to probe the synchrotron peak. With such refined constraints we should have a quite detailed knowledge of the bulk injection from the pulsar and its termination shock. In turn, it may be hoped that this, and similar measurements of other PWNe, will help us understand the physics of these relativistic outflows.

REFERENCES

Abdo, A. A., et al. 2009a, ApJ, 696, 1084
Abdo, A. A., et al. 2009b, ApJS, 183, 46
Abdo, A. A., et al. 2010, ApJ, 713, 154
Aharonian, F. A., et al. 2006, A&A, 448, L43
Alvarez, H., et al. 2001, A&A, 372, 636
Aschenbach, B., Egger, R., & Trumper, J. 1995, Nature, 373, 587
Atwood, W. B., et al. 2009, ApJ, 697, 1071
Blondin, J. M., Chevalier, R. A., & Frierson, D. M. 2001, ApJ, 563, 806
de Jager, O. C., Harding, A. K., & Strickman, M. S. 1996, ApJ, 460, 729
de Jager, O. C., Slane, P. O., & LaMassa, S. M. 2008, ApJ, 689, L125
Dodson, R., et al. 2003, ApJ, 596, 1137
Duncan, A. R., Stewart, R. T., Haynes, R. F., & Jones, K. L. 1996, MNRAS, 280, 252
Dwarakanath, K. S. 1991, A&A, 12, 199
Gaensler, B. M., & Slane, P. O. 2006, ARA&A, 44, 17
Hales, A. S., et al. 2004, ApJ, 613, 977
Harnden, F. R., & Gorenstein, P. 1973, Nature, 241, 107
Harnden, F. R., Jr., Grant, P. D., Seward, F. D., & Kahn, S. M. 1985, ApJ, 299, 828
Haslam, C. G. T., Salter, C. J., Stoffel, H., & Wilson, W. E. 1982, A&AS, 47, 1
Helfand, D. J., Gotthelf, E. V., & Halpern, J. P. 2001, ApJ, 556, 380
Horns, D., Aharonian, F., Santangelo, A., Hoffmann, A. I. D., & Masterson, C. 2006, A&A, 451, L51
Kanbach, G., et al. 1980, A&A, 90, 163
Kanbach, G., et al. 1994, A&A, 289, 855
LaMassa, S. M., Slane, P. O., & De Jager, O. C. 2008, ApJ, 689, L121
Large, M. I., Vaughan, A. E., & Mills, B. Y. 1968, Nature, 220, 340
Levine, A. M., et al. 1984, ApJS, 54, 581
Mangano, V., Massaro, E., Bocchino, F., Mineo, T., & Cusumano, G. 2005, A&A, 436, 917
Markwardt, C. B., & Ogelman, H. 1995, Nature, 375, 40
Markwardt, C. B., & Ogelman, H. B. 1997, ApJ, 480, L13
Mattox, J. R., et al. 1996, ApJ, 461, 396
Pellizzoni, A., et al. 2010, Science, 327, 663
Porter, T. A., Moskalenko, I. V., & Strong, A. W. 2006, ApJ, 648, L29
Rishbeth, H. 1958, Aust. J. Phys., 11, 550
Thompson, D. J., Fichtel, C. E., Kniffen, D. A., & Ogelman, H. B. 1975, ApJ, 200, L79
Wallace, P. T., et al. 1977, Nature, 266, 692
Weiler, K. W., & Panagia, N. 1980, A&A, 90, 269